Astronomy & Astrophysics manuscript no. papCtoO˙V5
August 12, 2018
© ESO 2018

Dust in brown dwarfs and extra-solar planets

V. Cloud formation in carbon- and oxygen-rich environments

Ch. Helling, D. Tootill, P. Woitke, and G. Lee

Centre for Exoplanet Science, SUPA, School of Physics and Astronomy, University of St. Andrews, North Haugh, St. Andrews, Fife, United Kingdom, KY16 9SS
email: ch80@st-and.ac.uk

Accepted 2012 ?, Received 2012 ?, in original from August 12, 2018

arXiv:1612.01863v1 [astro-ph.SR] 6 Dec 2016

ABSTRACT

Context. Recent observations indicate potentially carbon-rich (C/O>1) exoplanet atmospheres. Spectral fitting methods for brown dwarfs and exoplanets have invoked the C/O ratio as additional parameter but carbon-rich cloud formation modeling is a challenge for the models applied. The determination of the habitable zone for exoplanets requires the treatment of cloud formation in chemically different regimes.
Aims. We aim to model cloud formation processes for carbon rich exoplanetary atmospheres. Disk models show that carbon-rich or near-carbon-rich niches may emerge and cool carbon planets may trace these particular stages of planetary evolution.
Methods. We extend our kinetic cloud formation model by including carbon seed formation and the formation of C[s], TiC[s], SiC[s], KCl[s], and MgS[s] by gas-surface reactions. We solve a system of dust moment equations and element conservation for a pre-scribed DRIFT-PHOENIX atmosphere structure to study how a cloud structure would change with changing initial C/O_0=0.43 ... 10.0.
Results. The seed formation efficiency is lower in carbon-rich atmospheres than in oxygen-rich gases due to carbon being a very effective growth species. The consequence is that less particles will make up a cloud for C/O_0>1. The cloud particles will be smaller in size than in an oxygen-rich atmosphere. An increasing initial C/O ratio does not revert this trend because a much greater abundance of condensible gas species exists in a rich carbon environment. Cloud particles are generally made of a mix of materials: carbon dominates if C/O_0>1 and silicates dominate if C/O_0<1. 80-90% carbon is reached only in extreme cases where C/O_0=3.0 or 10.0.
Conclusions. Carbon-rich atmospheres would form clouds that are made of particles of height-dependent mixed compositions, sizes and numbers. The remaining gas-phase is far less depleted than in an oxygen-rich atmosphere. Typical tracer molecules are HCN and C_2H_2 in combination with a featureless, smooth continuum due to a carbonaceous cloud cover, unless the cloud particles become crystalline.

Key words. astrochemistry - Methods: numerical - Stars: atmospheres - Stars: low-mass, brown dwarfs

1. Introduction

Spectral observations of extrasolar planets reveal their chemical content which is linked to the planet's formation process but which is altered by the planetary evolution. Migration and disk evolution, however, may challenge the direct and easy linking of present-days observable composition and planet formation. A couple of observations point to the possibility of planets with carbon-rich atmospheres. Madhusudhan et al. (2011) suggested the WASP-12b has a carbon-rich atmosphere based on a day-side emission spectrum, despite its host star being oxygen-rich. This is based on a synthetic spectrum comparison derived for a parameterised atmosphere structure to fit the observations. Kreidberg et al. (2015) retrieve from HST transmission spectrum of WASP-12b the presence of H_2O with a C/O≈ 0.5 on the planet's day-side in contrast to Madhusudhan et al. (2011), and suggest an atmosphere with clouds and haze and absorption by e.g. CO, CH_4, HCN, C_2H_2, FeH. The planets HD 8988b,c,d,e have tentatively been suggested to show molecules (b & d: CH_4, C_2H_2, CO_2; c: C_2H_2; e: CH_4, C_2H_2; Oppenheimer et al. 2013) typical for carbon-rich atmospheres (Helling et al. 1996). Tsiaras et al. (2016) analyze WFC3 HST data for the super-Earth 55 Cancri e and derive a C/O=1.1 on this evaporating, probably hydrogen-rich planet. A tentative HCN detection is suggested. Jura et al. (2015) report on a polluted Keck/HIRES spectrum of the white dwarfs WD Ton 345 that suggest that the accreted disk planetisimals (debris of a disrupted planet) must have been carbon-rich and water-poor.

Disk chemistry simulations suggest that the local disk gas can become carbon-rich but only under special circumstances and at certain times (Helling et al. 2014; Ali-Dib et al. 2014; Eistrup et al. 2016). This suggests that carbon-rich planets could be a tracer of these rare episodes in an originally oxygen-rich disk. When planets form by the core-accretion scenario, smaller planetary masses would favor an enrichment with heave elements inside the core.

The dominating source of carbon (and Al and Li) in the universe are evolved stars that undergo the third dredge up on the asymptotic giant branch. Dust-driven winds (radiation pressure due to large luminosities) then enrich the ISM with these elements. Abia et al. (2003) show that solar-metallicity AGB stars with C/O∼1, and a C/O>2 are considered extreme. Nuclear synthesis and evolutionary models show that only low-metallicity AGB stars would produce C/O=10 (Abia et al. 2003). Given the low abundance of carbon-rich, nearly-sun-like stars (Fortney 2012), carbon-rich planets around those stars most likely must be linked to the disk evolution rather than to a primordial C/O>1. The situation may differ for planets around carbon-rich AGB stars which may well have been enriched by the dust that leaves the star in abundance during its wind phases with mass losses

of 10^{-7} ... 10^{-4}M$_\odot$ yr^{-1} (e.g. Schröder et al. 1998; Winters et al. 2003). The dominating source for carbon in the early universe, however, are Population III SNe ejecta. Carbon-rich planets could now form in situ as by-product of carbon-enhanced metal-poor stars (CEMPs), i.e. carbon-rich Pop II stars, as suggested by Mashian & Loeb (2016). Would such planets still have clouds? First investigations for metal-deficient ultra-cool atmospheres were done for oxygen-rich gases only but demonstrated that cloud do prevail to unexpected low metallicities of [M/H]≈-5.0 (Witte et al. 2009).

Linking spectra of extrasolar planets to planet formation and disk evolution requires therefore the possibility to treat oxygen-rich and carbon-rich atmospheres and the chemical transition from the one to the other. An essential part of this task is to be able to treat cloud formation in such chemically diverse environments. Also determining the habitable zone for extrasolar planets demands detailed cloud models across various chemical regimes (Yang et al. 2013; Barnes et al. 2016).

We present results from a kinetic cloud formation model treating seed formation, growth/evaporation, gravitational settling and element depletion to form cloud particles of height-dependent, mixed compositions and size in carbon-rich and oxygen-rich environments. We present first results from our next generation of cloud formation models which follow the moment approach presented in Woitke & Helling (2003, 2004); Helling & Woitke (2006); Helling et al. (2008). Section 2 summarizes our approach. Section 3 presents our results for clouds in atmospheric environments of changing C/O ratios from C/O<1 (oxygen-rich) to C/O>1 (carbon-rich), and presents how global cloud properties change with evolving C/O. One of the questions to be answered is under which conditions cloud particles would form primarily (> 80%) of pure carbon. Sections 4 and 5 present the results for the remaining gas-phase elements and discuss some example molecules, respectively. Section 6 summarizes this paper.

2. Approach

We present a new generation of our kinetic, non-equilibrium cloud formation model which allows us to investigate cloud structures in oxygen-rich and carbon-rich environments, and the transition between the two. We assess the impact of the carbon-to-oxygen ratio (C/O) on the resulting cloud structure details for giant gas planet atmospheres. We utilize example model atmosphere structures ($T_{\rm eff}$ = 1600 K and 2000K, log(g) = 3.0, initial solar metallicity) from the Drift-Phoenix atmosphere grid that is representative for the atmosphere of a giant gas planet. We use the model ($T_{\rm gas}$, $p_{\rm gas}$)-structure as input for our external cloud formation program Drift to derive the cloud structures details for different C/O-ratios by adjusting the carbon-abdundance. All other elements are kept at solar values. We present our results for a selected set of C/O ratios (0.43, 1.0, 1.1, 1.5). We assume that the planets form via the core-accretion scenario and that the accreted dust has already settled out and leaves behind an atmosphere with the respective C/O ratio.

2.1. Cloud formation model

Our cloud formation model describes the formation of clouds by nucleation, subsequent growth by chemical surface reactions on-top of the seeds, evaporation, gravitational settling, element conservation and convective replenishment (Woitke & Helling 2003, 2004; Helling & Woitke 2006; Helling et al. 2008; for a summery see Helling & Fomins 2013). The effect of nucleation, growth & evaporation on the remaining elements in the gas phase is fully accounted for (Eqs. 10 in Helling et al. 2008). The surface growth of a diversity of materials causes the cloud particles to grow to μm-sized particles of a mixed composition of those solids taken into account. Cloud particles size and material composition change with height in the atmosphere.

We have extended our model to allow a simultaneous treatment of multiple nucleation species (seed formation) and to allow for the formation and growth of mixes of carbonaceous and silicate materials. Please refer to the above references regarding the formula body of our cloud formation model.

Seed formation: The seed formation is described by classical nucleation theory which has been modified for TiO_2 nucleation to take into account knowledge about $(TiO_2)_N$ cluster formation (Jeong et al. 1999, 2000; Lee et al. 2015). We follow the approach, incl. all material constants, as described in Lee et al. (2015) for TiO_2 seed formation.

The second seed formation species that we take into account is carbon. We do not present any new development of carbon-nucleation but apply the approach used for AGB star wind modeling e.g. in Fleischer et al. 1992; Woitke 2006, but for the more complete gas-phase chemistry described in Bilger et al. (2013).

In an oxygen-rich gas (C/O= 0.43), we apply TiO_2 nucleation only as all carbon will be blocked in CO or CH_4. In a clearly carbon rich case (C/O= 1.1, 1.5, 3.0, 10.0), we apply carbon nucleation only as all oxygen will be locked up in CO. We demonstrate in Sect. 3.1.1 the simultaneous treatment of TiO_2 and C nucleation for the case C/O=1.0 where the required oxygen and carbon are not blocked by CO, and the gas phase composition becomes substantially more demanding.

Surface growth: The growth of the cloud particle bulk is described by gas-surface reactions between the gas and the cloud particle surface as described in Helling & Woitke (2006) and Helling et al. (2008). As different materials can become thermally stable at very similar temperatures, a mix of material will grow. The surface reactions that were used are summarized in Tables A.3 and A.2. For carbon-rich cases, we apply the set of surface reaction listed in Tables A.3, and for oxygen-rich cases Table A.2. The chemical transition case of equal carbon and oxygen abundances (C/O=1.0) is represented by Table A.2 with the addition of C[s], SiC[s], TiC[s], KCl[s] and MgS[s] from Tables A.3. The vapor pressure data used for the materials that were added to our cloud model (C[s], MgS[s], TiC[s], SiC[s], KCl[s]) are given in Table A.1.

2.2. Drift-Phoenix model atmosphere

Drift-Phoenix (Dehn 2007, Helling et al. 2008, Witte et al. 2009) model atmosphere simulations solve the classical 1D model atmosphere problem coupled to a kinetic phase-non-equilibrium cloud formation model. Each of the model atmospheres is determined by the effective temperature ($T_{\rm eff}$ [K]), the surface gravity (log(g) (with g in cm/s^2), and element abundances. The cloud's opacity is calculated applying Mie and effective medium theory.

The 1D atmosphere models provide atmospheric properties such as the local convective velocity, and the temperature-pressure ($T_{\rm gas}$ [K], $p_{\rm gas}$ [dyn/cm^2]) structure. The local temperature is the result of the radiative transfer solution, the local gas pressure of the hydrostatic equilibrium. For the lack of a con-

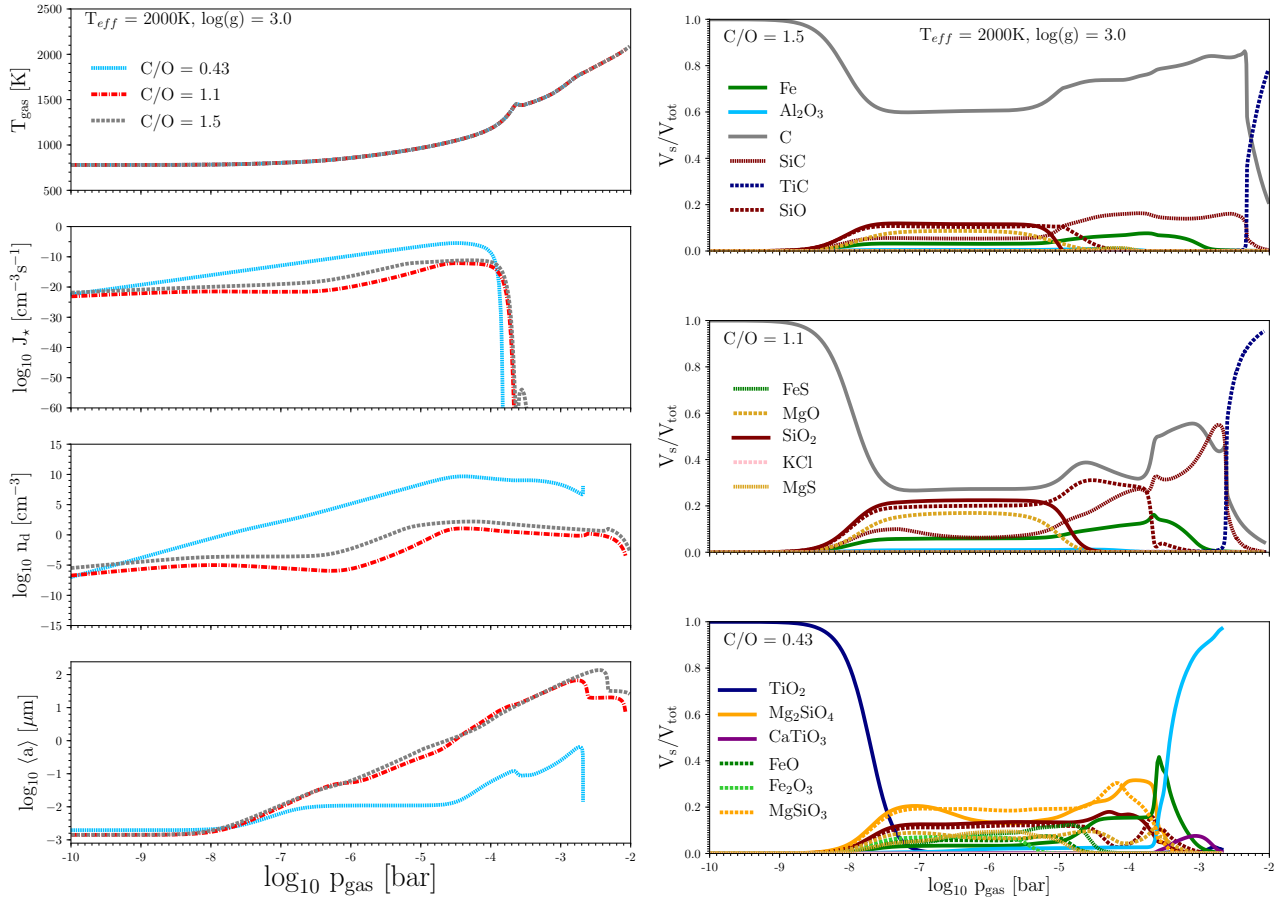

Fig. 1. Left: Cloud structures for changing C/O=0.43 (blue), 1.1 (red), 1.5 (grey) for a prescribed DRIFT-PHOENIX (T_{gas}, p_{gas}) structure for a giant gas planet with T_{eff} = 2000K, log(g)=3.0, initial solar element abundances. **1st panel:** input T_{gas} [K] and p_{gas} [bar], **2nd panel:** nucleation rate $\log J_*$ [cm^{-3}s^{-1}], **3rd panel:** cloud particle number density $\log n_d$ [cm^{-3}], **4th panel:** mean cloud particle radius $\log\langle a\rangle$ [μm].
Right: Changing material composition, V_s/V_{tot} [%] (relative volume fractions of solid species s) of the cloud particles with changing C/O ratio.

sistent solution as of yet, we apply the same oxygen-rich atmosphere structure in all tests presented in this paper.

3. Clouds in atmospheric environments of changing C/O ratio from C/O<1 to C/O>1

3.1. Changing cloud structures with changing C/O

The cloud structure of oxygen-rich giant gas planets and brown dwarfs is well understood based on kinetic cloud modeling (Helling & Fomins 2013; Helling & Casewell 2014), but it still depends on the basic material constants (e.g. vapor pressure, cluster data; Fortney et al. 2016) and poses a challenge as part of atmosphere model simulations (forward and retrieval) where it is most often parameterised. In a stationary scenario, haze-like small cloud particles made of a rich mix of silicates and metal-oxides populate the uppermost cloud layers. If they precipitated through the atmosphere, the cloud particles change their size and the material composition becomes dominated by Mg/Si/O materials with only small inclusions from iron and other oxides. The innermost cloud part is made of big particles with a mix of high-temperature condensates of which one is always dominating (e.g. TiO_2[s] or Fe[s]). This is the case for C/O=0.43 which is shown for reference in Fig. B.1 (right). This cloud structure is a refinement of the DRIFT-PHOENIX result as published in Witte et al. (2009).

Over-all cloud structure: Figure 1 (left) demonstrates how the cloud structure changes if the initial C/O ratio (C/O_0) changes from an oxygen-rich (C/O_0 <1) to a carbon-rich (C/O_0 >1) gas-composition. Such a drastic change in environmental chemistry can occur during disk evolution and also due to the set-in of dust formation (Helling et al. 2014). We present our results for C/O_0=0.43 (blue), 1.1 (red) and 1.5 (gray). Figure 1 (right) shows how the material composition of the cloud particles (in units of V_s/V_{tot} – relative volume fractions of solid species s) change.

The results from the second panel in Fig. 1 (left) show that the nucleation rate of TiO_2 (light blue line) in an oxygen rich environment exceed that of C in a carbon rich gas (red line) because carbon is initially considerably more abundant in the gas-phase and therefore growth very quickly onto the newly formed grain. This leads to a rapid decrease of carbon in the gas which causes the nucleation process to stop. An increase in C/O ratio to C/O_0=1.5, i.e. an increase of carbon, leads to a somewhat increased seed formation rate (gray) compared to the C/O_0=1.1 case.

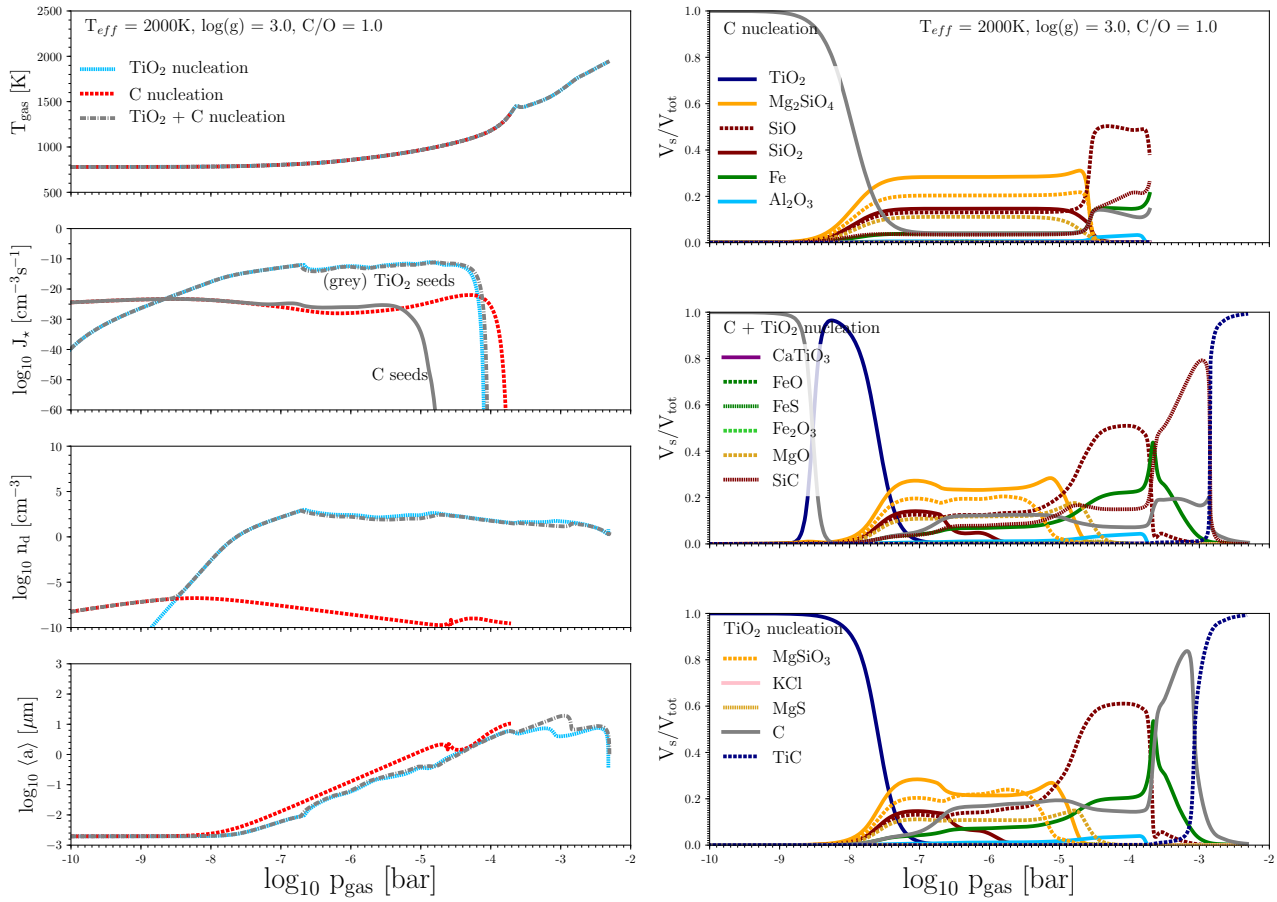

Fig. 2. Clouds formation at C/O=1.0 for a prescribed DRIFT-PHOENIX (T_{gas}, p_{gas}) structure for a giant gas planet with T_{eff} = 2000K, log(g)=3.0, initial solar element abundances. Three cases are tested: i) TiO_2 nucleation only (light blue) , ii) carbon nucleation only (red), iii) simultaneous carbon and TiO_2 nucleation (gray). **Left: 1st panel:** input T_{gas} [K] and p_{gas} [bar], **2nd panel:** nucleation rate log J_* [$cm^{-3}s^{-1}$], **3rd panel:** cloud particle number density log n_d [cm^{-3}], **4th panel:** mean cloud particle radius log$\langle a \rangle$ [μm]. **Right:** Changing material composition, V_s/V_{tot} [%] (relative volume fractions of solid species s) of the cloud particles for different nucleation species.

A larger nucleation rate will lead to more seeds forming and hence a larger number density of cloud particles n_d (Fig. 1, left, 3rd panel) for a given (T_{gas}, p_{gas})-structure. The nucleation rates reach their maximum at almost the same pressure level independent of the initial C/O ratio. This might change if carbon-cloud and temperature structure were consistently treated. The cloud extends below the nucleation regimes in all cases depicted in Fig. 1 (left, compare 2nd & 3rd panel) as the growing cloud particles gravitationally settle into deeper atmospheric layers.

The bottom panel of Fig. 1 (left) shows that the large number of seeds in the oxygen-rich case results in the smallest average cloud particles sizes, as now more surface area is available onto which a given number of gas species will grow. *As a result the cloud particles in a carbon rich environment are larger but less numerous.* It is interesting to note that the average particle size of cloud particles in carbon-rich environments does not appear to differ drastically between just carbon rich environments and more concentrated carbon rich environments, despite the latter having a higher number density by as as much as three orders of magnitude in places. This suggests that there exists a much greater abundance of potential condensible gas species in a rich carbon environment, such that the increased number density is canceled out.

Cloud composition: Figure 1 (right) (see also Fig. B.1 for comparison in more detail) presents what materials the cloud particles are made of, how their composition changes with height and how it changes with changing C/O_0-ratio. The plotted values, V_s/V_{tot}, are the relative volume fractions of the solid s and are calculated from Eqs.(3) in Helling et al. (2008). Of particular interest is the question if cloud particle in a carbon-rich atmosphere will remain homogeneous as commonly assumed for AGB star wind modeling (Fleischer et al. 1992; Mattsson et al. 2010; Wittkowski et al. 2016), or if they will be composed of some mix of materials similar to the chemically more complex oxygen-rich case.

In a heavily carbon rich atmosphere (here: C/O_0=1.5), the dominant dust component is C[s], with it making up at least 60% of the volume except for at the deepest atmospheric layers where TiC[s] becomes more prevalent. The top panel in Fig. 1 (right) also shows the emergence of SiC[s] in the inner atmosphere, where it becomes the second most abundant material between 10^{-5} bars and roughly $10^{-3.5}$ bars. Other significant components of the dust phase in the mid atmosphere are SiO[s], SiO_2[s] and MgO[s] reaching a volume fraction of ≈30% . Fe[s] appears in small amounts that increase somewhat when SiO[s], SiO_2[s] and MgO[s] have evaporated.
In comparison, a carbon rich atmosphere at a lower C/O ratio

(here: C/O_0=1.1), carbon, while still the most abundant dust component for most of the cloud layer, comprises as little as 30% of the dust volume once other materials begin to condense onto the cloud particles. The proportional increase of oxygen aids the condensation of oxygen bearing dust species, such as SiO[s], SiO_2[s] and MgO[s] in the mid cloud layer. SiO[s] exists for roughly an extra bar of pressure in depth compared to C/O_0=1.5. The abundance of SiC[s] also increases to a maximum of ≈ 50% of the dust volume at its peak, compared to just 20% for a C/O_0 =1.5. Also Fe[s] has increased its volume fraction to as much as 10. . . 15%.
In an oxygen rich environment (here: C/O_0=0.43) the seed particle TiO_2 is the prevalent species only during the nucleation period, in the upper-most cloud layers where dust growth does not occur efficiently. Once condensation onto the seed particles begins the dust volume instead comprises of a mixture of Mg_2SiO_4[s], $MgSiO_3$[s] and many other silicate and oxide species.

To summarize; the seed particle material comprises a much more significant fraction of the total dust volume in carbon rich cases, due to the higher elemental abundances of C compared to Ti. In both environments, silicon species seem to form a large portion of the dust, bonded to Mg and multiple O in the oxygen rich environments, and simply O or O_2 in the carbon rich.

3.1.1. The case of C/O_0=1.0

Disk evolution seems to suggest that a chemical situation where C/O≈1 is not uncommon. ProDiMo[1] (Woitke et al. 2009, 2016) chemical disk model results presented in Helling et al. (2014) suggest that at 10Myrs a C/O≈ 1.0 range appears between 1 . . . 10AU. While the exact number will depend on the model set up (and on the chemical rates applied), the C/O≈ 1.0-range may well be a common features during certain evolutionary disk stages, or even indicative of it. Assuming that the disk dust has settled onto/into the planets core and that the planet is cold enough that no outgasing occurs, the planet is then left with a C/O≈1.0 atmosphere. Hence, an evolving planet will have to go through this stage of evolution at some point in its life time. Here we use our cloud formation model to study the cloud details that occur should a planet be effected by the external disk C/O≈1 or achieve else-wise C/O≈1.

Modeling cloud formation in an atmosphere where carbon and oxygen appear in the same amounts and are locked up on CO is challenging because non of the well-studied cases (oxygen-rich and carbon-rich) can be used as guide. While it is not obvious which nucleation species to use (with the added challenge of the availability of material data), we use the case to perform some tests on the effect of the nucleation species on a potentially forming cloud. To do so, we perform three test: i) TiO_2 nucleation only , ii) carbon nucleation only, iii) simultaneous carbon and TiO_2 nucleation. All three test calculations use the same set of surface growth reactions in Table A.2 with the addition of C[s], SiC[s], TiC[s], KCl[s] and MgS[s] from Tables A.3. Hence, the only difference is how we treat the formation of seed particles.

Figure 2 shows how the different nucleation species affect the over-all cloud structure. The pure carbon-nucleation is the least efficient seed formation process in the case C/O=1.0, pure TiO_2 nucleation is the most efficient. The result is that pure carbon-seeds would lead to very few cloud particles (Fig. 2, left, 3rd panel, red dashed lines) as it occurs with 10 order of magnitudes less efficiency (2nd panel, red dashed lines). It might, however, be unexpected that the mean cloud particle radii (Fig. 2, left, 4th panel) differ by not too much. Figure 2 (right) demonstrate the material mix that can be expected for cloud particles forming from a gas of initially C/O=1. While the upper cloud deck is dominated by the seed forming species material, the remaining cloud where the surface growth causes the largest increase in grain size, is rather similar between the three cases shown in Fig. 2. Given that the nucleation process determines the whole cloud structure we suggest to use carbon- and TiO_2-nucleation in order to optimally represent the cloud structure in an atmospheres where C/O≈1. The details of the material composition will be discussed as part of our study of varying C/O in Sect.3.3.

[1] Radiation thermo-chemical models of protoplanetary disks

3.2. Decreasing $T_{\rm eff}$

Given the strong temperature dependence of the cloud formation processes, and in particular of the seed formation (see steep gradient of J_* in e.g. Figs. 1, 2), we examine the impact of decreasing $T_{\rm eff}$ of the atmosphere from 2000K to 1600K on the cloud structure and composition. The surface gravity remains the same at log(g) = 3.0, and initial solar element abundances for C/O_0=0.43, 1.1, 1.5 are studied.

Cloud Structure: Figure 3 shows for $T_{\rm eff}$=1600K (log(g)=3.0) the changes in the cloud structure moving from the oxygen rich environment (C/O_0 = 0.43) to carbon rich cases (C/O_0 = 1.1, 1.5). As for the previous case, the nucleation rate of TiO_2 (second panel, blue) in the oxygen rich case is greater than that of the carbon nucleation in either carbon rich atmosphere. Compared to $T_{\rm eff}$ = 2000K (Fig. 1) the nucleation rate is lower for all C/O ratios, but is particularly pronounced in mid cloud layer (10^{-7} to 10^{-5} bars) in the carbon rich environments where a dip in the nucleation rates of carbon seeds is observed. The nucleation rate is of the order of 10 (C/O_0 = 1.5) to 20 (C/O_0 = 1.1) magnitudes smaller. Nucleation of seed particles also continues for roughly a bar in depth deeper for all C/O regimes, compared with $T_{\rm eff}$ = 2000K.

The lower nucleation rates have a dramatic impact on the number density of cloud particles, particularly in the carbon rich cases. For the oxygen rich environment, there is a four order decrease in magnitude in the number density of cloud particles at the top of the cloud level at $T_{\rm eff}$ = 1600K compared to $T_{\rm eff}$ = 2000K, however, this difference becomes negligible deeper into the cloud structure. The number density increases at 10^{-5} bars (in the present model) for C/O_0 = 1.5 and 10^{-4} bars for C/O_0 = 1.1 due to increasing nucleation rates, which is more sharply pronounced than the slight increase present for $T_{\rm eff}$ = 2000K. The minor decrease in number density in the carbon rich regimes between 10^{-8} bars and $10^{-5}/10^{-4}$ bars is due to greater gravitational settling, caused by the increased grain size, causing more cloud particles to rain out to lower cloud levels than new seeds can replace.

As is expected, the average grain size (4th panel, Figs. 1, 3) remains much smaller in the oxygen rich environments, where there is extra competition for condensible material between the more numerous cloud particles, than for carbon rich environments. Additionally, given the vastly lower number density of cloud particles in an atmosphere with $T_{\rm eff}$ = 1600K, the cloud particles grow to much larger radii than in the $T_{\rm eff}$ = 2000K case. At the lower cloud levels, the average grain size is an order of magnitude greater than for $T_{\rm eff}$ = 2000K. As in the hotter envi-

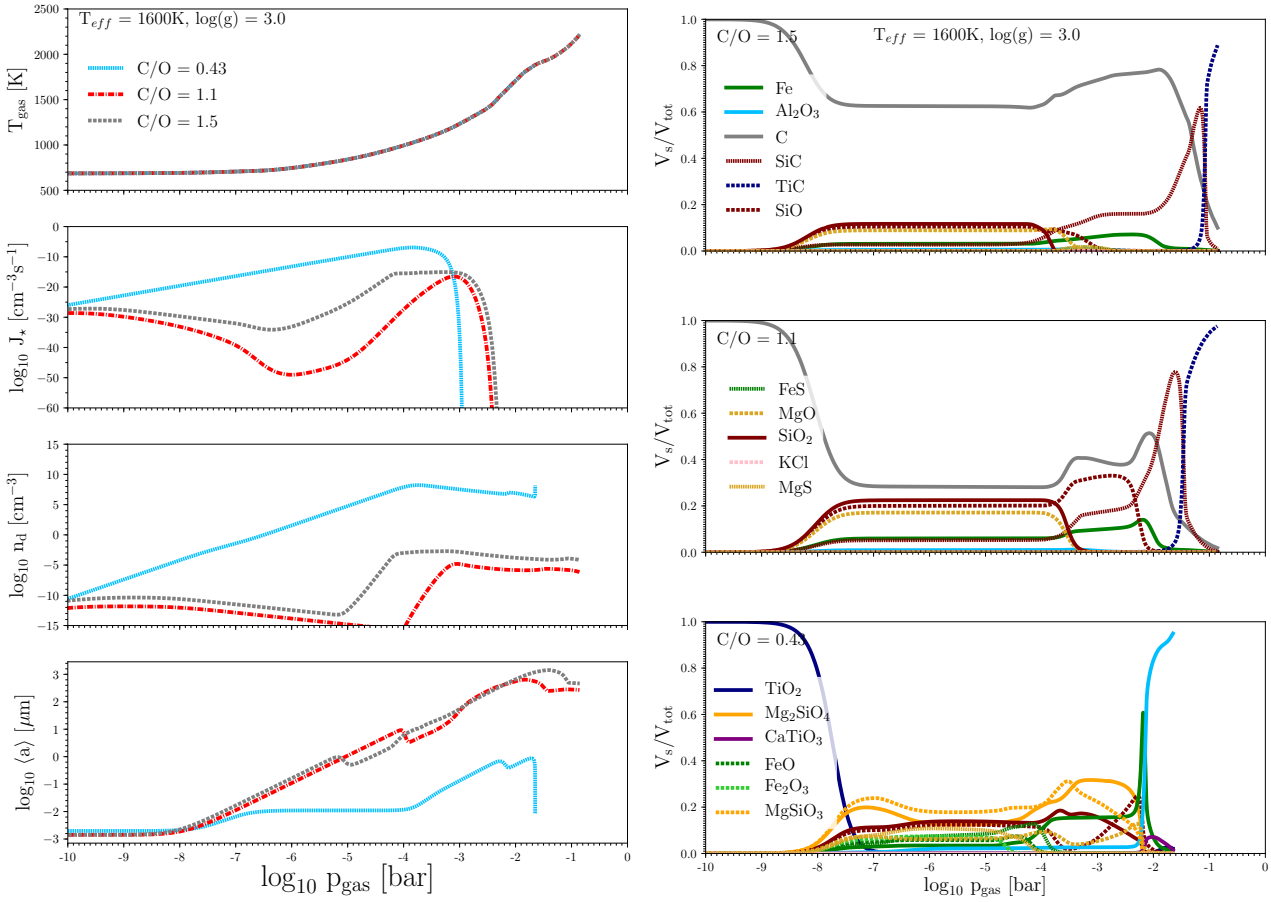

Fig. 3. Cloud structures for changing C/O=0.43 (blue), 1.1 (red), 1.5 (gray) for a prescribed DRIFT-PHOENIX (T_{gas}, p_{gas}) structure for a giant gas planet with T_{eff} = 1600K, log(g)=3.0, initial solar element abundances. **Left: 1st panel:** input T_{gas} [K] and p_{gas} [bar], **2nd panel:** nucleation rate log J_* [cm^{-3}s^{-1}], **3rd panel:** cloud particle number density log n_d [cm^{-3}], **4th panel:** mean cloud particle radius log$\langle a \rangle$ [μm].
Right: Changing material composition, V_s/V_{tot} [%] (relative volume fractions of solid species s) of the cloud particles for different nucleation species.

ronment however, the average grain size remains largely independent of the degree of carbon abundance.

Cloud Composition: Figure 3 shows the composition of the cloud particles throughout the cloud level. There is no change at the top of the cloud level with all the dust comprising of seed particle material. As in the T_{eff} = 2000K atmosphere there is a more significant decrease in the carbon fraction of the dust for the less carbon rich case. The condensation of other growth species again begins roughly 10^{-8} bars with silicate and magnesium compounds comprising the largest non carbon fractions of the dust (SiO[s], SiO_2[s] and MgO[s] for C/O$_0$ > 1; Mg_2SiO_4[s], $MgSiO_3$[s] and SiO_2[s] for C/O$_0$ < 1).

The composition of the dust in the bulk of the cloud structure, from 10^{-8} bars to 10^{-3} bars remain largely unchanged upon altering T_{eff}. The analysis of the differences between a carbon rich cloud composition and oxygen rich cloud composition presented in Section 3.1 hold in this region as well.

Changes in the cloud composition appear deep within the cloud layer. In the oxygen rich environment the is a larger spike in the volume fraction of Fe[s] prior to the sharp increase of Al_2O_3[s] which then becomes the dominant fraction. In the carbon rich environments SiC[s] becomes a major constituent of the dust volume, roughly 70% for C/O$_0$ = 1.5 and 80% at C/O$_0$ = 1.1. This compares to a maximum of roughly 15% for C/O$_0$ = 1.5 and 60% for C/O$_0$ = 1.1 for T_{eff} = 2000K. The SiC[s] in the dust replaces pure carbon suggesting that for cooler effective temperatures the deep cloud layers become richer in Si-binding species.

3.3. Global changes of cloud properties with changing C/O$_0$, incl. the Extreme

We demonstrate how the globally changing C/O ratio effects global cloud properties. This may be envisioned as an evolutionary C/O sequence from a typical oxygen-rich to a strongly carbon-rich environment. Two scenarios maybe envisison for such evolutionary C/O sequence: a) an AGB star enriching the planet when it evolved away from the main sequence, and b) a planet encountering chemically different acretion environemnts in a planet-forming disk. In this first study, we wish to derive global cloud trends for changing C/O ratios. We therefore also consider extreme values (C/O$_0$=3.0 and 10.0) which are guided by observations of carbon-rich Pop II stars (e.g. Table 1 in Mashian & Loeb 2016 and references therein). The results are summarizes in Table 3.2 and in Fig. 4.

Three C/O-regimes are considered: the oxygen rich regime (C/O$_0$ = 0.43 and 0.9), the transition regime (C/O$_0$ = 0.95, 1.0

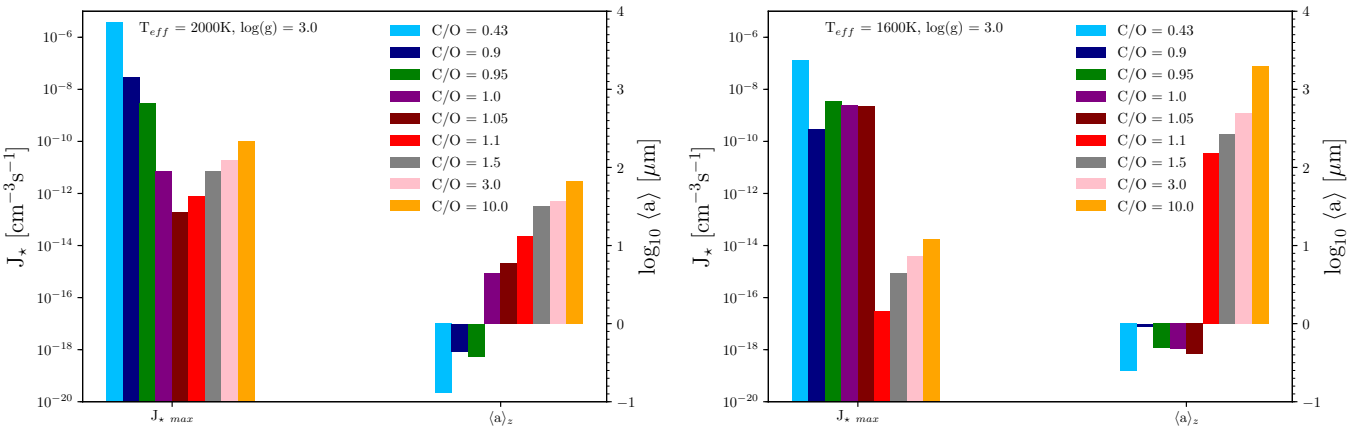

Fig. 4. Global changes of cloud structure: Changes in maximum nucleation rate throughout cloud layer (left cluster of bars) and average mean grain size throughout cloud layer (right cluster of bars). Data taken from range of C/O$_0$ ratios from 0.43 to 10.0. **Left** T$_{\rm eff}$ = 2000K and log(g) =3.0. **Right** T$_{\rm eff}$ = 1600K and log(g) =3.0.

Table 1. Numerical comparison of Cloud structure over range of C/O ratios. Top of Cloud Layer corresponds to $1.43 \cdot 10^{-12}$ bars, middle of cloud layer to 10^{-7} bars and bottom of cloud layer to between $1.37 \cdot 10^{-3}$ bars and $8.64 \cdot 10^{-2}$ bars, depending on the C/O ratio

		V$_s$/V$_{tot}$ top	middle	bottom
C/O$_0$	0.43	100% TiO$_2$	1.2% TiO$_2$	1.7% TiO$_2$
$J_{*,max}$	$4 \cdot 10^{-6}$		20.5% Mg_2SiO_4	97% Al_2O_3
[cm^{-3} s^{-1}]			11.2% SiO	0.4% Fe
$\langle a \rangle_{avg}$ [μm]	0.13		12.6% SiO$_2$	0.8% $CaTiO_3$
			19.3% $MgSiO_3$	
			6.1% Al_2O_3	
			5.5% FeO	
			4.5% FeS	
			7% Fe_2O_3	
			8.9% MgO	
			5.3% MgS	
C/O$_0$	0.9	100% TiO$_2$	1.2% TiO$_2$	5.2% TiO$_2$
$J_{*,max}$	$3 \cdot 10^{-8}$		25.1% Mg_2SiO_4	0.2% SiO
[cm^{-3} s^{-1}]			11.5% SiO	92% Al_2O_3
$\langle a \rangle_{avg}$ [μm]	0.44		12.9% SiO$_2$	1% Fe
			18.1% $MgSiO_3$	1.5% $CaTiO_3$
			0.6% Al_2O_3	
			5.9% FeO	
			2% FeS	
			7.5% Fe_2O_3	
			9.6% MgO	
			2.1% MgS	
C/O$_0$	0.95	100% TiO$_2$	1.2% TiO$_2$	4.6% SiO
$J_{*,max}$	$3 \cdot 10^{-9}$		26.1% Mg_2SiO_4	33.9% Al_2O_3
[cm^{-3} s^{-1}]			12% SiO	58.7% Fe
$\langle a \rangle_{avg}$ [μm]	0.38		13.5% SiO$_2$	1.5% $CaTiO_3$
			18.7% $MgSiO_3$	1.2% MgO
			6.3% FeO	
			6.8% Fe_2O_3	
			9.6% MgO	
			2.1% MgS	

and 1.05) and the carbon rich regime (C/O$_0$ = 1.1, 1.5, 3.0 and 10.0). The oxygen and carbon rich cases were treated with a single seed species (respectively TiO_2 and C) as described in Sect. 2.1. The transition region was treated with both seed species and an increased selection of growth species as described in Sect. 3.1.1.

We utilize the following properties to provide a global characterization of the cloud: the maximum nucleation rate, $J_{*,\rm max}$ [cm^{-3} s^{-1}], the average mean cloud particle size $\langle a \rangle_{\rm avg}$ [μm] (mean cloud particle radius, $\langle a \rangle$, averaged over whole vertical, 1D cloud extension), and three characteristic values for the cloud particles material composition (top, middle and bottom of cloud).

Maximum nucleation rate: The maximum nucleation rate, $J_{*,\rm max}$, within the cloud structure (left cluster of bars in Fig. 4) decreases as the initial C/O ratio approaches unity from the oxygen rich side. This is due to the decrease in oxygen not locked up in CO resulting in a gas phase abundance of TiO_2 with which to form seed particles. The maximum nucleation rate then increases again as the initial C/O increase above unity, again due to the increased abundance of gas phase seed material, in this case carbon. The maximum nucleation rate can be greater at unity than at C/O$_0$ = 1.05 due to the greater availability of TiO_2 in the gas phase with which to form seeds. TiO_2 is a more efficient seed forming species than C, which results in higher maximum nucleation rates even if the gas phase abundance of carbon is much greater (such as in the extreme C/O$_0$ = 10 compared with the slightly oxygen rich environment of C/O$_0$ = 0.9). This trend is also present for T$_{\rm eff}$ = 1600K (Fig. 4 right) though less pronounced in the transition regime (C/O$_0$ = 0.95, 1.0 and 1.05).

Average mean cloud particle size: The average mean grain size, $\langle a \rangle_{\rm avg}$, across the whole cloud layer (right cluster of bars on Fig. 4) shows an increasing trend with increasing global C/O$_0$. From previous sections, it was anticipated that the cloud particles present in the carbon rich atmosphere would be larger than those in the oxygen rich atmosphere, due to the decreased competition for condensible growth material as a result of less seed particles forming. The increase in the averaged mean grain size, $\langle a \rangle_{\rm avg}$, as the initial C/O ratio increases in the oxygen-rich regime is also cause by lower number densities of seed particles. The in-

Table 2. Numerical comparison of Cloud structure over range of C/O ratios. Top of Cloud Layer corresponds to $1.43 \cdot 10^{-12}$ bars, middle of cloud layer to 10^{-7} bars and bottom of cloud layer to between $1.37 \cdot 10^{-3}$ bars and $8.64 \cdot 10^{-2}$ bars, depending on the C/O ratio

		V_s/V_{tot} top	middle	bottom
C/O_0	1.0	100%	1.3% TiO_2	0.5% C
$J_{*,max}$	$7 \cdot 10^{-12}$	C	27.2% Mg_2SiO_4	99.3% TiC
[cm^{-3} s^{-1}]			12.5% SiO	0.1% Fe
$\langle a \rangle_{avg}$	4.47		14.1% SiO_2	
[μm]			3.8% Fe	
			19.5% $MgSiO_3$	
			10.9% MgO	
			5.6% C	
			4% SiC	
C/O_0	1.05	100%	1.4% TiO_2	4.3% C
$J_{*,max}$	$2 \cdot 10^{-13}$ C		25.5% Mg_2SiO_4	0.3% SiC
[cm^{-3} s^{-1}]			11.8% SiO	95.4% TiC
$\langle a \rangle_{avg}$	5.88		3.8% SiO_2	0.8% Fe
[μm]			18.3% $MgSiO_3$	
			10.1% MgO	
			11.3% C	
			4.2% SiC	
C/O_0	1.1	100%	5.9% Fe	4.3% C
$J_{*,max}$	$8 \cdot 10^{-13}$	C	0.5% Al_2O_3	0.3% SiC
[cm^{-3} s^{-1}]			26.7% C	95.4% TiC
a_{avg}	13.31		8.3% SiC	
[μm]			19.7% SiO	
			16.3% MgO	
			22.1% SiO_2	
C/O_0	1.5	100%	3.1% Fe	21.2% C
$J_{*,max}$	$7 \cdot 10^{-12}$	C	0.2% Al_2O_3	0.5% SiC
[cm^{-3} s^{-1}]			59.9% C	78.3% TiC
$\langle a \rangle_{avg}$	31.60		5.5% SiC	
[μm]			10.8% SiO	
			8.5% MgO	
			11.8% SiO_2	
C/O_0	3.0	100%	1.2% Fe	96.8% C
$J_{*,max}$	$2 \cdot 10^{-11}$	C	84.4% C	3.1% SiC
[cm^{-3} s^{-1}]			2.2% SiC	
$\langle a \rangle_{avg}$	36.56		4.1% SiO	
[μm]			3.3% MgO	
			4.5% SiO_2	
C/O_0	10.0	100%	0.3% Fe	99.5% C
$J_{*,max}$	$1 \cdot 10^{-10}$	C	96% C	0.4% SiC
[cm^{-3} s^{-1}]			0.6% SiC	
$\langle a \rangle_{avg}$	67.38		0.9% SiO	
[μm]			0.9% MgO	
			1.1% SiO_2	

creasing average mean particle size, $\langle a \rangle_{avg}$, with increasing initial C/O ratio in the carbon-rich regime, however, may not be explained by this reasoning as the nucleation rate also increases as the initial C/O ratio increases. Therefore, the increased $\langle a \rangle_{avg}$ are instead the result of increased availability of growth material, specifically with regards to carbon as a growth species. This is a conjecture supported by the high proportion of carbon present in the dust composition of cloud particles at almost every part of the cloud layer, as presented in the top two panels of Fig. 1 (right).

Dust Composition: The upper level of the cloud layer for every initial C/O ratio is made of the respective seed material. For the transition regime (C/O_0 = 0.95, 1.0 and 1.05), the C/O ratio decides which seed condenses first with C/O < 1 producing TiO_2 seeds and C/O>= 1 producing carbon seeds. The cloud particle volume in the middle of the cloud layer is made of numerous materials. In the oxygen rich and transition regimes the largest fraction of the volume are Mg_2SiO_4[s], $MgSiO_3$[s], SiO[s] and SiO_2[s]. The percentage of Mg_2SiO_4[s] grows slightly as the C/O_0 increases with the small fraction of Al_2O_3[s] present at C/O_0 = 0.43 becoming negligible as the C/O_0 ratio increases. In contrast, the largest components of the normal carbon rich environments (C/O_0 = 1.1 and 1.5) replace the fractions of Mg_2SiO_4[s] and $MgSiO_3$[s] with larger proportions of SiO[s], SiO_2[s] and MgO[s] as well C[s]. As the C/O_0 ratio increases, the fraction of C[s] increases too at the expense of SiO[s], SiO_2[s] and MgO[s]. This trend is continued to the extreme C/O_0 ratios of 3.0 and 10.0 where the dust volume at the middle of the cloud layer is almost completely comprised of carbon. At the bottom of the cloud layer more stable dust species such as Al_2O_3[s] dominate in the oxygen rich regime, though with volume fractions that decrease as the C/O_0 ratio increase with increasing fractions of Fe[s] becoming present, most notably when C/O_0 = 0.95. If $C/O_0 \geq 1$, TiC[s] becomes the major material of the cloud particles, but decreases as the initial C/O increases, with C[s] becoming more prevalent, indeed dominating the volume fraction at extreme initial C/O ratios (3.0, 10.0).

3.4. Extreme C/O_0

We briefly examine the cloud structure and cloud composition of atmospheres extremely rich in carbon (C/O_0 = 3.0, 10.0). Only such extremely carbon-rich cases produce cloud or dust particles that are made almost entirely of carbon with only very little inclusions of other materials. These results are not only of interest for planetary atmosphere research but also for modeling the ISM enrichment through AGB star winds and the enrichment of the early universe due to SNe ejecta (e.g. Mashian & Loeb 2016). In particular the in situ formation of carbon-rich planets in the early universe as by-product of CEMP stars would occur at $C/O_0 > 10.0$ (Table 1 in Mashian & Loeb 2016).

Cloud Structure: Figure 5 illustrates the cloud structure in extremely carbon rich environments. The general trend of the nucleation rate (top panel), number density (second panel) and average grain size (third panel) appear to be very similar to those presented for C/O_0 = 1.1 and 1.5 in Fig. 1, though somewhat larger. This is expected for the nucleation rate (higher C/O ratio equates to a larger abundance of potential seed material in gaseous C) and hence the number density. The increased grain sizes is again caused by the increased abundance of growth material (here: carbon). It is interesting to note that increasing the C/O_0 ratio dramatically from 3.0 to 10.0 does not cause dramatic changes in the cloud structure, a one order of magnitude in the grain number density in the the upper half of the cloud layer being the most notable difference.

Dust Composition: A dramatic effect of the increased initial C/O ratio from 3.0 to 10.0 is seen however, in Fig. 5 (right). This figure is demonstrating the dust composition in the extreme carbon rich environments. At C/O_0 = 10.0, no less than roughly 95% of the dust volume is carbon at any point in the cloud layer,

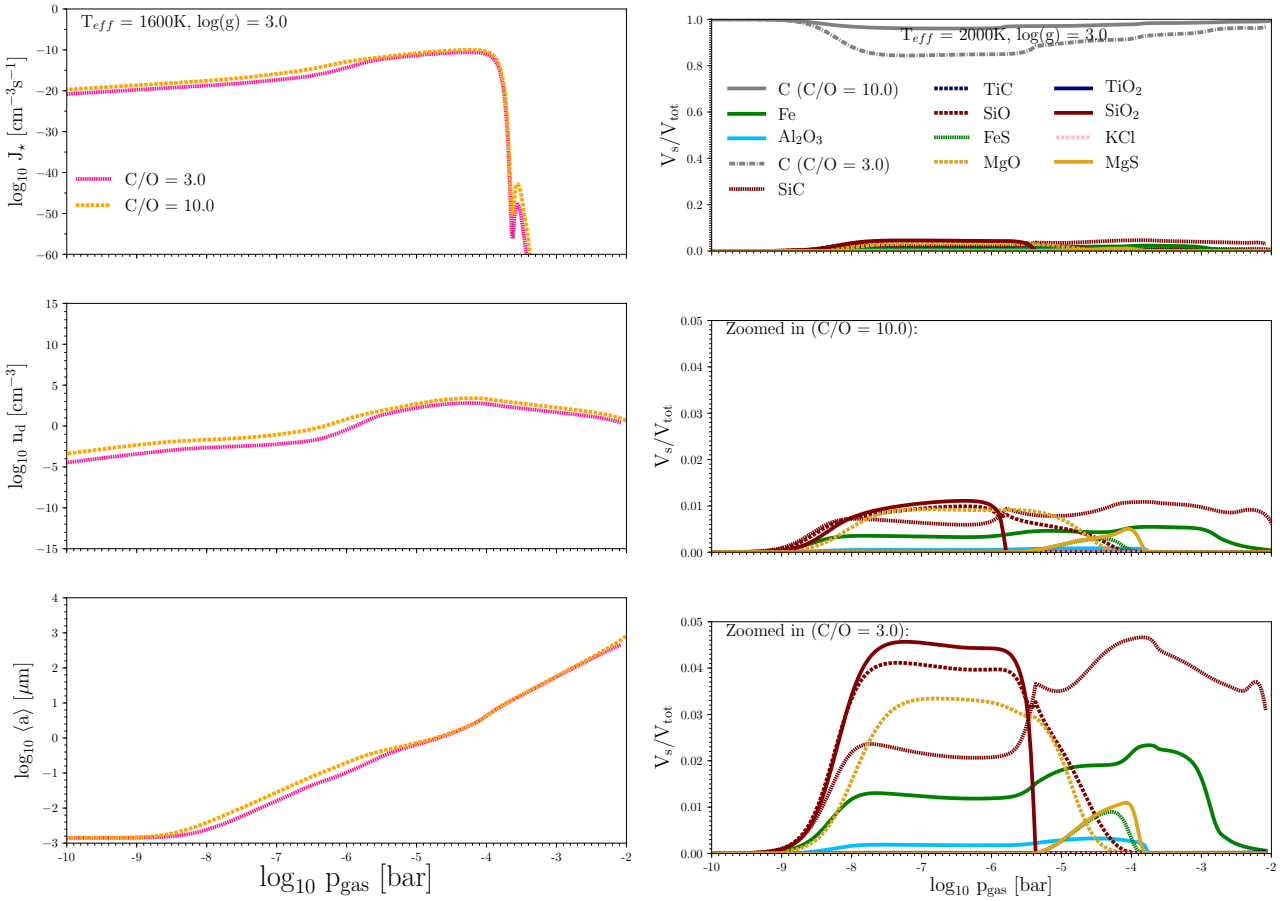

Fig. 5. Left: Cloud structures for changing C/O=3.0 (pink), 10.0 (orange) for a prescribed DRIFT-PHOENIX (T_{gas}, p_{gas}) structure for a giant gas planet with T_{eff} = 2000K, log(g)=3.0, initial solar element abundances. **1st panel:** nucleation rate log J_* [cm^{-3}s^{-1}], **2nd panel:** cloud particle number density log n_d [cm^{-3}], **3rd panel:** mean cloud particle radius log$\langle a \rangle$ [μm].
Right: 1st panel Changing material composition, V_s/V_{tot} [%] (relative volume fractions of solid species s) of the cloud particles for C/O ratios = 3.0 and 10.0.

with SiO[s], SiO_2[s], SiC[s] and MgO[s] making up only 1% of the remaining fraction each in the lower and middle cloud (2nd panel of Fig. 5 r.h.s.; this is a zoom-in of the 1st panel). In contrast, when the C/O_0 =3.0 the carbon fraction drops to roughly 85% of the total volume in the upper middle portion of the cloud, with Panel 3 showing SiO_2[s] and SiO[s] fractions around 4 times greater than present in C/O_0 = 10.0 and a MgO[s] fraction roughly 3 times as large. In the lower portions of the cloud, these fractions evaporate and are replaced by a SiC[s] and Fe[s] with each roughly a 4 times greater fraction than their equivalent fractions in the C/O_0 = 10.0 case.

4. Element depletion

The element abundances, ϵ_x, determine the chemical composition of the atmospheric gas from which the cloud particles form. The cloud formation processes reduce the element abundances through nucleation and surface growth or enrich them where evaporation occur. We therefore study the effect of a changing C/O_0 ratio on the element abundances remaining in the gas phase after the cloud particles have formed. All element abundances are plotted in comparison to the initial, solar element abundances (straight solid line) with ϵ_C adjusted according to the C/O_0 ratio. Figure 6 (left, panels depict different ranges) show how differently the elements that participate in cloud formation are depleted if the C/O_0 = 0.43, 1.0, 1.1, 1.5.

The by orders of magnitude largest element depletion for the C/O_0 ratios studied here occurs for C/O_0=0.43, i.e. in the oxygen-rich case for Si, S, Ti, Mg, O, Fe, Al, and Ca. This is supported by our findings that a considerably larger number of cloud particles composes a cloud in an oxygen-rich compared to a carbon-rich cloud atmosphere, despite remaining smaller in size. The element depletion becomes generally smaller when approaching C/O_0=1.0 (compare C/O_0=1.5, 1.1, 1.0), and increases again when the case is clearly carbon-rich like e.g. for C/O_0=1.5. The larges carbon-depletion occurs for C/O_0=1.5 as now the carbon contributes the largest volume fraction until its thermal stability limit near to bottom of the cloud. Somewhat more cloud particles form for C/O_0=1.5 compared to C/O_0=1.1 which does affect the element depletion (see Fig. 1).

Different nucleation species affect the chemical feedback on the gas phase differently. Ti is the most depleted element in the oxygen-rich case, while carbon remains moderately abundant even at very high C/O_0. An interesting case occurs in the transition regime where C/O_0 ≈1.0. Here, carbon-nucleation alone is insufficient in describing element depletion. Both, TiO_2 nucleation and the simultaneous consideration of carbon and TiO_2 (C + TiO_2) produce very similar results, only that the simultaneous C + TiO_2 nucleation leads to a somewhat stronger depletion of

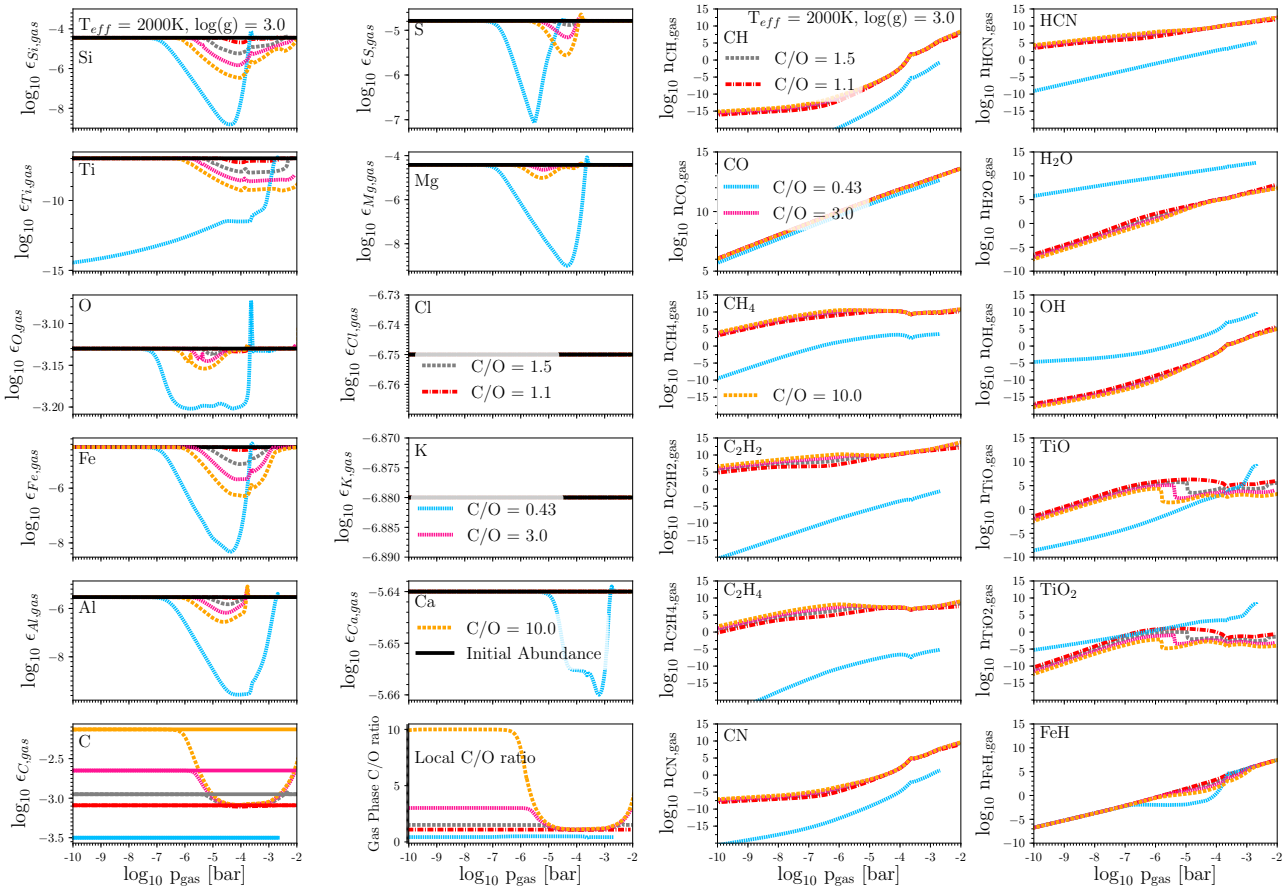

Fig. 6. Remaining gas-phase chemistry after cloud formation: **Left:** depleted gas element abundances after cloud formation. **Right:** Molecular abundances of a selected number of species to demonstrate the differences between the oxygen-rich (blue) and the carbon-rich cases. The underlaying atmosphere model is the same as in Fig. 1 with T_{eff}=2000K, log(g)=3.0 and initial solar abundances with the carbon adjusted according to the C/O ration listed.

Ti, and to less depletion of Fe, Al, S, and Ca. These differences are, however, very small.

K and Cl are not depleted for non of the C/O_0 ratios considered. This is in agreement with that KCl material volume fraction $\approx$ 0 in Fig. 1 and 2 (both r.h.s.). KCl is therefore a super-inefficient growth species in the temperature regime represented by our T_{eff}=2000K, log(g)=3.0 (oxygen-rich, initial solar element abundances) DRIFT-PHOENIX model atmosphere.

4.1. The local C/O ratio

The last row in Figures 6 (left panel right column) also shows the local, height-dependent C/O ratio for different global, initial C/O_0 ratios=0.43, 1.0, 1.1., 1.5., 3.0 and 10.0. These results combine the depleted oxygen and the carbon abundances effected by cloud formation. We find that the carbon-depletion in the carbon-rich cases makes the atmosphere locally somewhat more oxygen-rich by decreasing the locale C/O ratio. The largest change in the local C/O occurs for the highest value considered, C/O_0=10. All carbon-rich cases approach approximately the same local C/O$\approx$ 1.0 in the atmospheric region with the strongest carbon depletion. This is also apparent from ϵ_C in the same figure (left column). The evaporation of the carbon at the cloud bottom leads to a small increase of the C/O ratio above the initial value which is strongest for the highest C/O_0. As the oxygen-abundance decreases by cloud formation in oxygen-rich atmospheres, the local C/O ratio increases somewhat. This has been discussed in Bilger et al. (2013) for different global parameters (T_{eff}, log(g), [M/H]). Helling et al. (2014) demonstrated that oxygen-depletion for a global C/O=0.99 can lead to a substantial increase in C/O locally.

5. The abundances of gas phase molecules

Oxygen-rich gases (incl. CO, H_2O) and carbon-rich gases (incl. CO, CH_4) are dominated by different molecules (Fig. 6). CO blocks the oxygen in carbon-rich gases and the carbon in oxygen-rich gases, unless the gas pressure is too high. In cool atmospheres with high densities, CH_4 becomes the most important carbon-binding species. Figure 6 (right) shows the CO blocking works well in the case studied here.

Figure 6 further demonstrates the abundance of a number of selected molecules after cloud formation has reduced the element abundances as shown in Fig. 6: H_2O is the dominating oxygen-binding molecule regardless of the oxygen-depletion. TiO drops in abundance substantially and would produce a false-positive of a carbon-rich atmosphere due to the strong Ti depletion as result of cloud formation. The initial low Ti element abundances make TiO a good tracer for chemical effects on the atmospheric oxygen reservoir: TiO traces well the oxygen-depletion in the center of the cloud also in carbon-rich atmospheres (yellow to red lines), and the oxygen-enrichment at the bottom of the cloud in the oxygen-rich case (blue lines). The TiO

abundance returns to undepleted oxygen-rich values only when cloud particles evaporation has caused a considerable oxygen enrichment (see peak - blue line - on ϵ_O on left of Fig. 6). FeH, as one example for metal-hydrate molecules, does reflect the Fe-depletion in the oxygen-rich case. Fe[s] contributes only with 1 ... 3% to the particle volume in the carbon-rich cases, hence, causing only little effect on the FeH abundance. All other hydrates that bind elements , that participate into cloud formation, show a similar behavior. Metal hydrates can therefore appear relatively stronger in a spectrum of a cloud-forming atmosphere.

A carbon-rich atmosphere is dominated by more complex molecules like HCN, CH_4 and CO, with small carbo-hydrates like C_2H_2 and C_2H_4 increasing in abundance with increasing carbon-content. Despite C_2H_2 being more abundant than CN, CN has a larger absorption cross section and it would therefore be easier picked up from a spectrum (see Fig. 9 in Helling et al. 2000).

6. Concluding remarks

We present the first cloud formation model that is applicable to 1D atmosphere simulations of carbon-rich planetary objects. Carbon-rich atmospheres of planets might indicate a particular chemical niche during the chemical evolution of a protoplanetary disk. Carbon-planets, however, were also suggested to form in the early universe as by-product of Pop II stars. However, observing those might only be possible of they e.g. emerge as free-floating planets nearby.

Clouds forming in carbon-rich atmosphere differ from their oxygen-rich counterparts in that less cloud particles form which grow to larger sizes and a large fraction of their material is made of carbon. Similar to the oxygen-rich case, the cloud properties change with height and the cloud particles are made of a mix of materials. Cloud particles can only be nearly-homogeneous if the initial C/O ratio is $\sim$ 10.0. Such high C/O ratios are so far predicted from low-metallicity theoretical AGB star models or for carbon-enhanced metal-poor stars.

When cloud particles rain (gravitational settle) into the deeper atmosphere, they encounter increasing densities and increasing temperatures. The increasing densities increase the thermal stability of the materials and speed up the growth process due to an increase of surface reactions. The temperature, however, will allow the material to restructure into well-ordered matrices as pointed out by Helling & Rietmeijer (2009). Therefore, amorphous materials like carbon can turn into its crystalline counterpart, i.e. into diamonds, which would cause drastic change of optical properties during the cloud formation process. Clouds on super-carbon-rich planets may therefore effect the spectral appearance far less than in their oxygen-rich counterparts.

Carbon dust has been studied in great detail to understand the enrichment of the ISM by stellar winds on the AGB which yield the pre-courser for star and planet formation. Andersen et al. (1999) demonstrate that the extinction coefficient of amorphous carbon has no spectral feature for $\lambda > 0.3\mu$m (their Fig. 1), the exact value depending somewhat on the data source used. Silicon carbide (SiC[s]) is another material that forms from AGB star winds which has been identify from a broad emission feature 11 ... 11.5μm (Sect. 3.3 in Andersen et al. 1999, Suh 2000). However, aromatic 3.3 μm PAH feature and the aliphatic sub-features in the range of 3.4 ... 3.6μm were observed in the ISM and interpreted as a mix of HAC and PAH absorption representing small dust grains (Gadallah et al. 2013). The transmission spectrum of the hot Jupiter WASP-12b is almost completely flat. The optical slope appears considerably shallower compared to HD 189744b (Sing et al. 2016). While it is almost impossible that pure carbon can condense in any oxygen-rich atmosphere based on an equilibrium gas-phase chemistry composition, carbon and carbonaceous material appears in abundance if C/O>1. It might therefore be thinkable that either i) the atmosphere of WASP-12b is indeed carbon-rich as the detection of HCN and C_2H_2 would suggest, or ii) the original atmosphere was nearly carbon-rich and an efficient cloud formation tipped it over in the carbon-rich regime (like in Fig. 9 in Helling et al. 2014, or iii) external irradiation (e.g cosmic rays) drives a strong ion-neutral chemistry which leads to the emergence of larger carbo-hydrate molecules (Rimmer et al. 2014).

Acknowledgements. We highlight financial support of the European Community under the FP7 by an ERC starting grant number 257431. A summer scholarship for DT provided by the Royal Astronomical Society is highly acknowledged.

References

Abia C., Domínguez I., Gallino R., Busso M., Straniero O., de Laverny P., Wallerstein G., 2003, PASA, 20, 314
Ali-Dib M., Mousis O., Petit J.-M., Lunine J. I., 2014, ApJ, 785, 125
Andersen A. C., Loidl R., Höfner S., 1999, A&A, 349, 243
Barnes R., Deitrick R., Luger R., Driscoll P. E., Quinn T. R., Fleming D. P., Guyer B., McDonald D. V., Meadows V. S., Arney G., Crisp D., Domagal-Goldman S. D., Lincowski A., Lustig-Yaeger J., Schwieterman E., 2016, ArXiv e-prints
Bilger C., Rimmer P., Helling C., 2013, MNRAS, 435, 1888
Eistrup C., Walsh C., van Dishoeck E. F., 2016, ArXiv e-prints
Fleischer A. J., Gauger A., Sedlmayr E., 1992, A&A, 266, 321
Fortney J. J., 2012, ApJ, 747, L27
Fortney J. J., Robinson T. D., Domagal-Goldman S., Skålid Amundsen D., Brogi M., Claire M., Crisp D., Hebrard E., Imanaka H., de Kok R., et al. 2016, ArXiv e-prints
Gadallah K. A. K., Mutschke H., Jäger C., 2013, A&A, 554, A12
Helling C., Casewell S., 2014, A&A Rev., 22, 80
Helling C., Dehn M., Woitke P., Hauschildt P. H., 2008, ApJ, 675, L105
Helling C., Fomins A., 2013, Philosophical Transactions of the Royal Society of London Series A, 371, 20110581
Helling C., Jorgensen U. G., Plez B., Johnson H. R., 1996, A&A, 315, 194
Helling C., Rietmeijer F. J. M., 2009, International Journal of Astrobiology, 8, 3
Helling C., Winters J. M., Sedlmayr E., 2000, A&A, 358, 651
Helling C., Woitke P., 2006, A&A, 455, 325
Helling C., Woitke P., Rimmer P. B., Kamp I., Thi W.-F., Meijerink R., 2014, Life, 4
Helling C., Woitke P., Thi W.-F., 2008, A&A, 485, 547
Jeong K. S., Chang C., Sedlmayr E., Sülzle D., 2000, Journal of Physics B Atomic Molecular Physics, 33, 3417
Jeong K. S., Winters J. M., Sedlmayr E., 1999, in Le Bertre T., Lebre A., Waelkens C., eds, Asymptotic Giant Branch Stars Vol. 191 of IAU Symposium, Dust formation in oxygen-rich circumstellar shells around long–period variables. p. 233
Jura M., Dufour P., Xu S., Zuckerman B., Klein B., Young E. D., Melis C., 2015, ApJ, 799, 109
Kreidberg L., Line M. R., Bean J. L., Stevenson K. B., Désert J.-M., Madhusudhan N., Fortney J. J., Barstow J. K., Henry G. W., Williamson M. H., Showman A. P., 2015, ApJ, 814, 66
Lee G., Helling C., Giles H., Bromley S. T., 2015, A&A, 575, A11
Madhusudhan N., Harrington J., Stevenson K. B., Nymeyer S., Campo C. J., Wheatley P. J., et al. 2011, Nature, 469, 64
Mashian N., Loeb A., 2016, MNRAS, 460, 2482
Mattsson L., Wahlin R., Höfner S., 2010, A&A, 509, A14
Morley C. V., Fortney J. J., Marley M. S., Visscher C., Saumon D., Leggett S. K., 2012, ApJ, 756, 172
Oppenheimer B. R., Baranec C., Beichman C., Brenner D., Burruss R., Cady E., Crepp J. R., Dekany R., Fergus R., Hale D., Hillenbrand L., et al. 2013, ApJ, 768, 24
Rimmer P. B., Helling C., Bilger C., 2014, International Journal of Astrobiology, 13, 173
Schröder K.-P., Winters J. M., Arndt T. U., Sedlmayr E., 1998, A&A, 335, L9
Sharp C. M., Huebner W. F., 1990, ApJS, 72, 417
Sing D. K., Fortney J. J., Nikolov N., Wakeford H. R., Kataria T., Evans T. M., Aigrain S., Ballester G. E., Burrows A. S., Deming D., Désert J.-M., Gibson N. P., et al. 2016, Nature, 529, 59

Suh K.-W., 2000, MNRAS, 315, 740
Tsiaras A., Rocchetto M., Waldmann I. P., Venot O., Varley R., Morello G., Damiano M., Tinetti G., Barton E. J., Yurchenko S. N., Tennyson J., 2016, ApJ, 820, 99
Winters J. M., Le Bertre T., Jeong K. S., Nyman L.-Å., Epchtein N., 2003, A&A, 409, 715
Witte S., Helling C., Hauschildt P. H., 2009, A&A, 506, 1367
Wittkowski M., Chiavassa A., Freytag B., Scholz M., Höfner S., Karovicova I., Whitelock P. A., 2016, A&A, 587, A12
Woitke P., 2006, A&A, 452, 537
Woitke P., Helling C., 2003, A&A, 399, 297
Woitke P., Helling C., 2004, A&A, 414, 335
Woitke P., Kamp I., Thi W.-F., 2009, A&A, 501, 383
Woitke P., Min M., Pinte C., Thi W.-F., Kamp I., Rab C., Anthonioz F., Antonellini S., Baldovin-Saavedra C., Carmona A., Dominik C., et al. 2016, A&A, 586, A103
Yang J., Cowan N. B., Abbot D. S., 2013, ApJ, 771, L45

Appendix A: Surface growth reactions and vapor pressure data

The sets of surface reaction are provided here which have been applied to model oxygen-rich and carbon-rich cloud particle growth by gas-surface reactions as outlined in Helling et al. (2008). The cloud particle growth in a clearly oxygen-rich environment (e.g. C/O=0.43) is described by the surface reaction listed in Table 1 in Helling et al. (2008) plus those listed in Table A.2 in the present paper, adding to a total of 73 surface reactions. For the carbon rich case, we use 84 surface reactions which include the reactions for TiO_2[s], SiO_2[s], SiO[s], Fe[s], FeS[s], MgO[s], and Al_2O_3[s] (32 reactions) as listed in Table 1 in Helling et al. (2008) plus those given in Table A.3.

Table A.1 contains the vapor pressure data used for the materials that were added to our cloud model (C[s], MgS[s], TiC[s], SiC[s], KCl[s]). C[s], TiC[s], and SiC[s] are fits to the JANAF table (1986). MgS[s] is taken from Sharp & Huebner (1990), and KCl[s] from Eq. (18) in Morley et al. (2012).

Appendix B: More detailed results

Figure B.1 provides more detailed results of the cloud structures for the initial C/O ratios 0.43, 1.1, 1.5 the results of which were presented in Sect. 3. The plots in Fig. B.1 have the same set-up like in our previous publication to allow for a sensible comparison of cloud structures forming in different atmospheric conditions. The plots allow for a more detailed comparison between the oxygen-rich and the carbon-rich cloud formation.

Table A.1. Monomer volumes $V_{0,s}$ of solid materials from and fit coefficients c_i for the calculation of the saturation vapor pressures and difference Gibbs free energies. (*): done for this paper from JANAF tables (1986) – (**): Sharp & Huebner (1990), (***) Morley et al 2012.

condensate	$V_{0,s}$ [10^{-23} cm^3]	c_1	c_2	c_3	c_4	c_5	fit of	
C[s]	1.002	1.01428E+6	−7.23043E+5	1.63039E02	−1.75890E-3	9.97416E08	ln p_{sat}	(*)
MgS[s]	3.296	−7.93442E+4	−1.83584E+5	6.33920	−8.89360E-4	0.0	$\Delta G'$	(**)
TiC[s]	2.018	1.11878E+5	−1.37612E+6	3.20666E+2	−4.63379E-3	1.85306E-7	$\Delta G'$	(*)
SiC[s]	2.074	6.73337E+5	−1.24381E+6	3.21779E+2	−4.54405E-3	2.69711E-7	$\Delta G'$	(*)
KCl[s]	6.227	7.611 - 11382.0/T_{gas}					log p_{sat}	(***)

Table A.2. Oxygen-rich cloud formation: Dust growth surface reactions for a oxygen-rich environment in addition to those listed in Table 1 in Helling et al. (2008). This set of 73 reactions is applied for all oxygen-rich models in the present paper.

Index r	Solid s	Surface reaction	Key species
61	KCl[s]	KCl → KCl[s]	KCl
62	sylvite	KOH + HCl → KCl[s] + H_2O	min{KOH, HCl}
63		HK + HCl → KCl[s] + H_2	min{HK, HCl}
64		KOH + CaCl → KCl[s] + CaOH	min{KOH, CaCl}
65	MgS[s]	MgS → MgS[s]	MgS
66	niningerite	2 MgH + 2 FeS → 2 MgS[s] + H_2 + 2 Fe	min{MgH, FeS}
67		2 MgH + 2 H_2S → 2 MgS[s] + 3 H_2	min{MgH, H_2S}
68		2 MgOH + 2 H_2S → 2 MgS[s] + 2 H_2O + 1 H_2	min{MgOH, H_2S}
69		MgOH + CaS → MgS[s] + CaOH	min{MgOH, CaS}
70		MgO + CS → MgS[s] + CO	min{MgO, CS}
71		2 MgH + 2 CS → 2 MgS[s] + H_2 + 2 C	min{MgH, CS}
72		MgO + H_2S → MgS[s] + H_2O	min{MgO, H_2S}
73		Mg + H_2S → MgS[s] + H_2	min{Mg, H_2S}

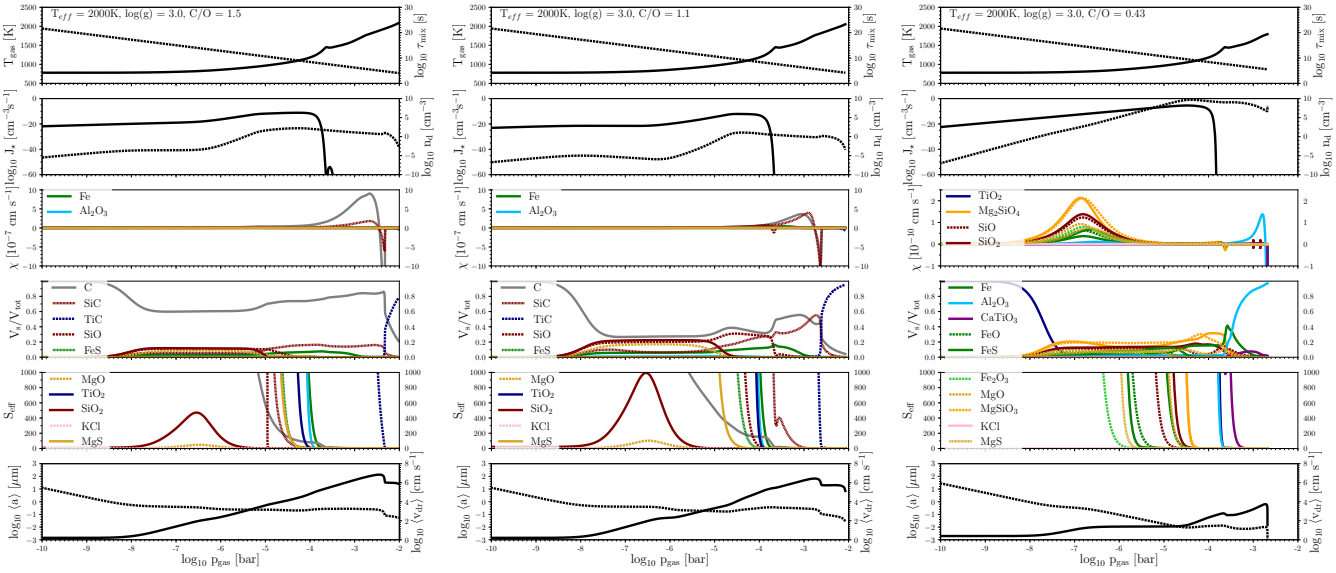

Fig. B.1. Detailed information about the cloud structure forming in an atmospheric gas with initial C/O ratios of 0.43, 1.1, 1.5 and a pre-scribed DRIFT-PHOENIX atmosphere profile for T_{eff} = 2000K and log(g)=3.0. **1st rows:** local gas temperature T_{gas} [K] (solid, left), mixing time scale τ_{mix} [s] (dashed, right); **2nd rows:** seed formation rate J_* [cm^{-3}s^{-1}]$(solid, left)$, number density of cloud particles n_d [cm^{-3}] (right, dashed), **3rd rows:** net growth velocity for individual materials s; **4th rows:** volume fraction V_s/V_{tot} for material s; **5th rows:** effective supersaturation ratio Seff for each material s; **6th rows:** mean cloud particles radius $\langle a \rangle$ [μm], drift velocity v_{drift} [cm s^{-1}] with respect to the local $\langle a \rangle$. The colour code is the same for all panels. All quantities are plotted versus the local gas pressure p_{gas} [bar].

Table A.3. Carbon-rich cloud formation: Dust growth surface reactions for a carbon-rich environment in addition to those listed in Table 1 in Helling et al. (2008) for TiO_2[s], SiO_2[s], SiO[s], Fe[s], FeS[s], MgO[s], and Al_2O_3[s] (32 reactions). This set of 84 reactions is applied for all carbon-rich models.

Index r	Solid s	Surface reaction	Key species
33	C[s]	$C \rightarrow C[s]$	C
34	carbon	$C_2 \rightarrow 2\ C[s]$	C_2
35		$C_3 \rightarrow 3\ C[s]$	C_3
36		$2\ C_2H \rightarrow 4\ C[s] + H_2$	C_2H
37		$C_2H_2 \rightarrow 2\ C[s] + H_2$	C_2H_2
38		$CH_4 \rightarrow C[s] + 2\ H_2$	CH_4
39	TiC[s]	$Ti + C \rightarrow TiC[s]$	min{Ti, C}
40	titanium-	$2\ Ti + C_2 \rightarrow 2\ TiC[s]$	min{Ti, C_2}
41	carbide	$3\ Ti + C_3 \rightarrow 3\ TiC[s]$	min{Ti, C_3}
42		$4\ Ti + 2\ C_2H \rightarrow 4\ TiC[s] + H_2$	min{Ti, C_2H}
43		$2\ Ti + C_2H_2 \rightarrow 2\ TiC[s] + H_2$	min{Ti, C_2H_2}
44		$Ti + CH_4 \rightarrow TiC[s] + 2\ H_2$	min{Ti, CH_4}
45		$TiC \rightarrow TiC[s]$	TiC
46		$TiS + C + H_2 \rightarrow TiC[s] + H_2S$	min{TiS, C}
47		$2\ TiS + C_2 + 2\ H_2 \rightarrow 2\ TiC[s] + 2\ H_2S$	min{TiS, C_2}
48		$3\ TiS + C_3 + 3\ H_2 \rightarrow 3\ TiC[s] + 3\ H_2S$	min{TiS, C_3}
49		$4\ TiS + 2\ C_2H + 3\ H_2 \rightarrow 4\ TiC[s] + 4\ H_2S$	min{TiS, C_2H}
50		$2\ TiS + C_2H_2 + H_2 \rightarrow 2\ TiC[s] + 2\ H_2S$	min{TiS, C_2H_2}
51		$TiS + CH_4 + H_2 \rightarrow TiC[s] + H_2S$	min{TiS, CH_4}
52		$TiC_2 \rightarrow TiC[s] + C$	TiC_2
53	SiC[s]	$Si + C \rightarrow SiC[s]$	min{Si, C}
54	silicon-	$2\ Si + C_2 \rightarrow 2\ SiC[s]$	min{Si, C_2}
55	carbide	$3\ Si + C_3 \rightarrow 3\ SiC[s]$	min{Si, C_3}
56		$4\ Si + 2\ C_2H \rightarrow 4\ SiC[s] + H_2$	min{Si, C_2H}
57		$2\ Si + C_2H_2 \rightarrow 2\ SiC[s] + H_2$	min{Si, C_2H_2}
58		$Si + CH_4 \rightarrow SiC[s] + 2\ H_2$	min{Si, CH_4}
59		$SiC \rightarrow SiC[s]$	SiC
60		$SiS + C + H_2 \rightarrow SiC[s] + H_2S$	min{SiS, C}
61		$2\ SiS + C_2 + 2\ H_2 \rightarrow 2\ SiC[s] + 2\ H_2S$	min{SiS, C_2}
62		$3\ SiS + C_3 + 3\ H_2 \rightarrow 3\ SiC[s] + 3\ H_2S$	min{SiS, C_3}
63		$4\ SiS + 2\ C_2H + 3\ H_2 \rightarrow 4\ SiC[s] + 4\ H_2S$	min{SiS, C_2H}
64		$2\ SiS + C_2H_2 + H_2 \rightarrow 2\ SiC[s] + 2\ H_2S$	min{SiS, C_2H_2}
65		$SiS + CH_4 + H_2 \rightarrow SiC[s] + H_2S$	min{SiS, CH_4}
66		$Si_2C \rightarrow SiC[s] + Si$	Si_2C
67		$SiC_2 \rightarrow SiC[s] + C$	SiC_2
68		$SiH_4 + C \rightarrow SiC[s] + 2\ H_2$	min{SiH_4, C}
69		$2\ SiH_4 + C_2 \rightarrow 2\ SiC[s] + 4\ H_2$	min{SiH_4, C_2}
70		$3\ SiH_4 + C_3 \rightarrow 3\ SiC[s] + 6\ H_2$	min{SiH_4, C_3}
71		$3\ SiH_4 + 2\ C_2H \rightarrow 4\ SiC[s] + 9\ H_2$	min{SiH_4, C_2H}
72		$2\ SiH_4 + C_2H_2 \rightarrow 2\ SiC[s] + 5\ H_2$	min{SiH_4, C_2H_2}
73		$SiH_4 + CH_4 \rightarrow SiC[s] + 4\ H_2$	min{SiH_4, CH_4}
74	KCl[s]	$KCl \rightarrow KCl[s]$	KCl
75	sylvite	$HK + HCl \rightarrow KCl[s] + H_2$	min{KH, HCl}
76		$2\ CKN + 2\ H_2O + CaCl_2 \rightarrow 2\ KCl[s] + 2\ C + N_2 + Ca(OH)_2 + H_2$	min{CKN, $CaCl_2$}
77	MgS[s]	$MgS \rightarrow MgS[s]$	MgS
78	niningerite	$2\ MgH + 2\ H_2S \rightarrow 2\ MgS[s] + 3\ H_2$	min{MgH, H_2S}
79		$2\ MgOH + 2\ H_2S \rightarrow 2\ MgS[s] + 2\ H_2O + H_2$	min{MgOH, H_2S}
80		$MgOH + CaS \rightarrow MgS[s] + CaOH$	min{MgOH, CaS}
81		$2\ MgN + 2\ H_2S \rightarrow 2\ MgS[s] + 2\ H_2 + N_2$	min{MgN, H_2S}
82		$2\ MgH + 2\ CS \rightarrow 2\ MgS[s] + H_2 + 2\ C$	min{MgH, CS}
83		$2\ MgOH + 2\ TiS \rightarrow 2\ MgS[s] + H_2 + 2\ TiO$	min{MgOH, TiS}
84		$Mg + H_2S \rightarrow MgS[s] + H_2$	min{Mg, H_2S}